Investigation of Flow Turning in a Natural Blockage Thrust Reverser

S. Hall, R.K. Cooper, E. Benard, S. Raghunathan
School of Aeronautical Engineering, Queen's University Belfast
David Keir Building, Stranmillis Rd, Belfast BT9 5AG, UK
s.l.hall@qub.ac.uk, r.cooper@qub.ac.uk, e.benard@qub.ac.uk, s.raghunathan@qub.ac.uk

Keywords: Thrust Reverser, Internal Flow

Abstract:

Experimental and computational low speed tests have been conducted on a 50% scale model of a two-dimensional natural blockage fan flow cascade thrust reverser. The aim of the work is to provide a reference database for future work investigating innovative flow control in fan flow thrust reversers. Results are presented for a reverser with cascade solidity = 1.3. The experimental nozzle pressure ratio must be increased to obtain relevant quantitative data. In addition the 2D computational results highlight problems of simulating a flow with 3D effects.

Introduction

Virtually all modern jet transport aircraft incorporate thrust reverser systems which are primarily used to provide an extra safety margin during landings and aborted take offs[1]. Thrust reversers operate by redirecting the engine exhaust flow forwards to produce a braking force. Unlike wheel braking systems their performance is not degraded by wet/icy runway conditions. Several types of thrust reverser are in operation today however this paper considers only the natural blockage cascade type fan flow thrust reverser which is used on the CF-34-8C powerplant of the Bombardier Aerospace CRJ-700/900 Regional Jet aircraft. The nacelle fan duct of the CF-34-8C engine is S-shaped. When the thrust reverser is deployed the rear section of the nacelle cowling translates aft to naturally block the fan duct whilst simultaneously exposing the reverser cascade opening in the side of the nacelle[2]. The fan flow is blocked and diverted outwards through the cascade opening where the cascade vanes deflect it forwards to produce the reverse thrust efflux (see figure 1).

It may be possible to use partial-cascade or cascadeless flow turning to achieve similar levels of reverse thrust. In the long term it may even be possible to design a thrust reverser with no moving parts which is essentially blockerless and cascadeless. Such a design would yield advantages in terms of reduced weight, reduced activation time and reduced leakage and pressure losses in the nacelle. The removal of the cascade from the system will necessitate its replacement with innovative fluidic flow control to ensure that flow turning through the reverser is maintained. Before investigating this possibility it is important to first understand the flow in the conventional natural blockage thrust reverser. This paper presents results from recent experimental and numerical studies of flow through a conventional natural blockage thrust reverser conducted at Queen's University Belfast. These studies form the basis to ongoing research within the school into innovative flow control in thrust reversers.

Methodology

The wind tunnel has a constant speed fan motor and the flow velocity can be set by partially blanking the fan inlet duct. Downstream of the fan there are four gauze screens for flow smoothing and a two-dimensional contraction section of contraction ratio 0.24. Following the contraction is the test section which measures 380mm by 89mm in cross-section. The maximum velocity in the test section is approximately 20m/s. The experimental model is a 50% scale two-dimensional simplified geometry representing the CF-34-8C thrust reverser in its deployed state. The cascade vanes are of constant thickness with blunt leading and trailing edges and have a design discharge angle of 45^0. The blocker surface is modelled as a simple flat plate (see figure 2). In a cross-sectional plane located at 125mm from the duct entrance six static pressure tappings are arranged in the duct walls with even spacing (two per wall). A total pressure rake consisting of thirteen probes is mounted in a sliding traverse in the duct roof. The rake vertically spans the duct and can be moved manually across the duct by means of the traverse. The constant cross-section duct is connected to the thrust reverser model by a set of bellows so that force measurements may be made on the reverser model at a later date. An exit pressure rake consisting of 26 probes (6 static probes, 19 total pressure probes and 1 directional alignment probe)[3] is mounted spanwise above the exit plane of the cascade. It can be manually rotated about its main centreline and using the alignment probe can be set to the local exit flow direction. The rake attachment consists of two slotted bars mounted on a spanwise axle. This allows the spanwise rake to be moved longitudinally relative to the model duct exit plane and also to be moved vertically to various heights above the exit plane.

Within the model duct several series of static pressure tappings are placed on the upper and lower surfaces. On the upper surface 16 tappings are placed along the centreline of the model. The positions of these tappings are shown in figure 3. On the lower surface a series of 15 tappings is placed along the centreline and an additional series of 15 tappings span the surface. In the spanwise series the tappings are located at 25mm intervals with the end tappings each being 15.5mm from the duct wall. The spanwise set of tappings will help to ascertain the degree of two-dimensionality of the flow and the effects of the sidewalls on the lower surface flow. In the longitudinal series the tappings are placed in denser concentrations in areas where flow separation is predicted to occur i.e. close to the blocker door on the lower surface and around the sharp corner at the inlet ramp. The pressure values from the various tappings and rakes are recorded manually from an inclined multi-tube manometer.

A CFD simulation of the experimental test is carried out using the commercial flow solver, FLUENT 6™. The CFD code is based on first order upwind difference operators on a two-dimensional, steady, implicit solution of the full Reynolds averaged Navier-Stokes (RANS) equations. The viscous turbulence model used is the RNG (renormalization group) k-ε model. Because of the low velocities involved in the case to be modelled the flow is assumed to be incompressible with the flow density set to the experimental atmospheric air density.

The computational grid is unstructured and is composed of 46726 cells. The farfield limits of the domain are set 20 model lengths upstream from the model, 10 model lengths downstream from the model and 20 model lengths vertically above the model. Figure 9 shows details of the computational thrust reverser model geometry. The main thrust reverser inflow is set as a velocity inlet boundary condition corresponding to the experimental velocity. The farfield boundaries are all set with pressure outlet boundary conditions equal to the experimental atmospheric pressure. In initial test runs it was found that the reverser efflux from the cascade was turned and attached to the wall upstream of the cascade exit. This effect does not occur in reality because the reverser efflux entrains flow into the low pressure region beneath the efflux. In the present 2D computational model this is simulated by creating an inflow of 5% of the experimental velocity on the upstream wall which injects flow vertically into the domain (see figure 9). The scheme converges after 1500 iterations.

It should be noted that the CFD analysis is still in early development. At the time of publication grid independence studies have yet to be carried out. However the CFD results to date are presented to show general trends and comparisons with the experimental data.

Results and Discussion

Results are presented for the case of cascade solidity (σ) of 1.3 at six different mean inlet velocities: 8.5m/s, 9.5m/s, 10.8m/s, 12m/s, 12.4m/s, 13.3m/s. For each case the nozzle pressure ratio, defined as the ratio of inlet total pressure to atmospheric pressure is calculated. Static pressure is measured longitudinally on the upper and lower surfaces along the model centreline and also on the lower surface a spanwise static pressure distribution is measured. At a plane above the cascade exit a spanwise survey of total pressure is taken for the case of inlet velocity 13.3m/s. In addition the two-dimensional direction of the exit flow streamlines are determined at the centre span. The pressure data is presented in terms of pressure coefficients:-

$$C_p = \frac{P - P_a}{\frac{1}{2}\rho U_{ref}^2}$$

Where P_a is the atmospheric pressure datum and U_{ref} is a notional isentropic nozzle velocity. This is obtained from an assumed isentropic expansion through the nozzle for the velocity 13.3m/s case. Based on this assumption U_{ref} =1.76 U_m where U_m is the measured mean inlet velocity. The use of pressure coefficients should collapse the data for various flow rates to a single curve because of the low Mach number of the experiment and, hopefully, a small effect due to Reynolds number. The Reynolds number is defined in terms of the duct hydraulic diameter and inlet velocity.

For the tunnel velocity variation the nozzle pressure ratio was found to vary from 1.0013-1.0033. The low nozzle pressure ratio is due to the low velocities of the tests. Literature on other experimental test programs typically quote nozzle pressure ratio ranges of 1.1-2.0 to be comparable with full-scale flow conditions.

Figures 4 and 5 show the surface static pressure distributions on the centreline of the top and bottom surfaces of the internal duct. On the bottom surface the initial decrease of pressure coefficient suggests that the flow accelerates around the curvature of the bottom surface. The pressure coefficient then increases suggesting that the flow slows as it travels along the following straight duct section . Figure 5 shows the static pressure levelling off at the position of static port number 12. This may imply flow separation away from the bottom surface of the duct as it approaches the blocker corner. On the top surface of the duct (figure 4) the increasing pressure coefficient indicates that the flow slows as it moves around the initial curvature and following straight duct section. As it approaches the inlet ramp the flow accelerates rapidly as shown by the rapid decrease in pressure coefficient here. There is an adverse pressure gradient around the inlet ramp and separation occurs at approximately the position of port number 10 after which the pressure is approximately constant.

Figure 6 shows the spanwise static pressure distribution across the bottom surface of the duct. There are small variations in the static pressure which may be due to the beginnings of corner vortices and/or surface irregularities at the duct inlet due to the bellows.

At the front and rear of the cascade exit the flow is degraded as shown by the lower spanwise total pressure coefficient distributions (traverse position x=170mm and x=80mm respectively, figure 7). Over the middle of the cascade (x=90mm to x=150mm) the flow rate is higher and there is little change in the flow with longitudinal position. In similar experiments Thompson[6] noted that the cascade vanes at the aft of the cascade have relatively little effect as the flow here is being turned internally by the flow blocker surface. Similarly the flow at the front of the cascade is relatively unaffected by the foremost cascade vane. The degraded flow at the front and rear of the cascade is supported by the measurement of centre-span flow direction at the traverse plane (figure 8). At x=170mm the flow is overturned to deflection angle 26^0 whilst over the middle section of the cascade the flow is deflected to approximately $40\text{-}45^0$ which is very close to the design discharge angle of the vanes. Flow overturning is caused by the flow adhering to the convex trailing edge of the cascade vanes as observed by Poland[4]. Romine and Johnson [5] also noted that losses in the thrust reverser are a function of the cascade effective area. As deflection angle decreases the cascade effective area decreases leading to increased flow blockage and a drop in flow discharge. This could account for the degraded flow at the first exit rake traverse position in figure 7. The pressure coefficient data shows that over the middle of the cascade pressure losses are less than 20%.

A CFD simulation of the experimental test with inlet velocity 13.3 m/s (NPR=1.0033) has been conducted. Figure 10 shows velocity vectors of the flow through and leaving the thrust reverser geometry. The regions of increased flow around the curvatures and the region of reduced flow velocity at the junction of the bottom wall and flow blocker surface are clearly visible as is the efflux jet exiting the cascade at approximately 45^0. Figures 11 and 12 show a comparison of the experimental and computational results for static pressure distribution on the bottom and top walls of the reverser duct. In figure 11 the static pressure is given at positions along the bottom wall corresponding to the horizontal distance relative to the inlet (x). There is a problem with the same scheme for the upper wall since at the inlet ramp the wall doubles back on itself. Therefore in figure 12 the positions located after the inlet ramp apex are presented in terms of a modified horizontal distance. The apex of the inlet ramp on the upper surface is defined as x_{max} = 0.174m as shown in figure 12. The modified horizontal distance is expressed as the apex distance plus the modulus of the distance from the apex to the post-apex position in question.

From figure 11 and 12 it can be seen that on the duct walls the experimental static pressure coefficients are higher than those predicted by the computational scheme. The fact that the difference in pressure coefficient between experimental and computational results is approximately 0.15 on the bottom wall but only 0.1 on the top wall is as yet unexplained. The computational scheme appears to capture the variation of static pressure with wall position very well except for the flow separation occurring at the inlet ramp and bottom wall/flow blocker junction. The difference in static pressure coefficient between the experimental and computational results indicates that in the experiments more pressure is required to drive the flow. This may be due to a combination of three-dimensional factors which are not present in the two-dimensional model. Such factors may include the affect of corner vortices on the bottom surface and reduced flow turning through the duct. Reduced flow turning would give a less uniform flow at the cascade resulting in a reduction of cascade efficiency. Hence a larger pressure difference would be required to maintain the mass flow rate through the duct.

It is also suggested that the flow separation on the inlet ramp contributes to the higher driving pressure in the experiments. The relationship between this separation and the aforementioned three-dimensional effects is still not fully understood. In an attempt to deliberately make the 2D computational model simulate the separation the flow from the inlet ramp the ramp surface was made notionally porous. The variation in static pressure distribution for this deliberate porous alteration is also shown in figures 11 and 12. The region of separation on the inlet ramp is more accurately captured and as a result of the separation the pressure coefficient over the main duct is increased. This appears to corroborate the earlier suggestion that the ramp separation is a factor leading to the increased pressure required to drive the experimental flow. From figure 11 the additional porosity has virtually no affect on the static pressure coefficient on the bottom wall.

.

Conclusion

The experiment successfully models the qualitative aspects of the flow through the reverser in terms of efflux deflection angle and pressure distributions. However the nozzle pressure ratio range for the experiments is set too low for quantitative data collection. It is suggested that the tunnel velocity is increased to rectify the problem.

The preliminary CFD results highlight the problems of attempting to computationally model in 2D a flow which is highly 3D in nature. Generating a 3D computational model would reduce the need to make artificial alterations to correctly simulate the three-dimensional effects in the thrust reverser. This could potentially offset the inherent added complexity and computation time of such a model.

Bibliography

1. Yetter, J.A., *Why do airlines want and use thrust reversers? - A compilation of airline industry responses to a survey regarding the use of thrust reversers on commercial transport airplanes*, NASA TM-109158, January 1995

2. Short Brothers PLC (GB), *Aircraft Propulsive Power Unit Thrust Reverser with Separation Delay Means*, UK patent no. GB231481, November 2000.

3. Ower, E. and Pankhurst, R.C., *The Measurement of Air Flow*, Pergamon Press, Oxford, 1966.

4. Poland, D.T., *Aerodynamics of Thrust Reversers for High Bypass Turbofans*, AIAA paper 67-418, July 1967.

5. Romine, B.M. and Johnson, W.A., *Performance Investigation of a Fan Thrust Reverser for a High Bypass Turbofan Engine*, AIAA-84-1178, AIAA/SAE/ASME 20th Joint Propulsion Conference, Cincinnati, OH., June 11-13, 1984.

6. Thompson, J.D., *Thrust Reverser Effectiveness on High Bypass Ratio Fan Powerplant Installations*, SAE Paper, Ref. 660736, October 1966.

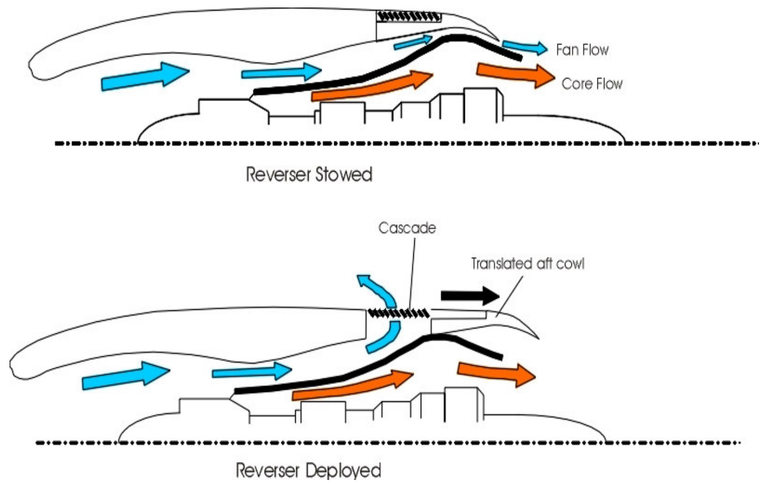

Figure 1. Natural Blockage Thrust Reverser

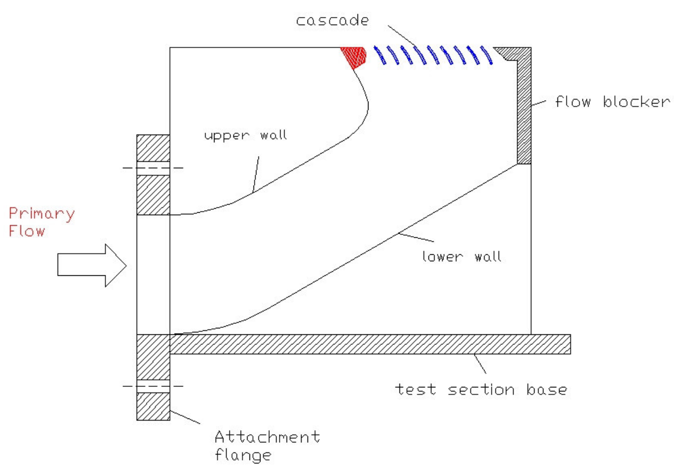

Figure 2. The Experimental Model

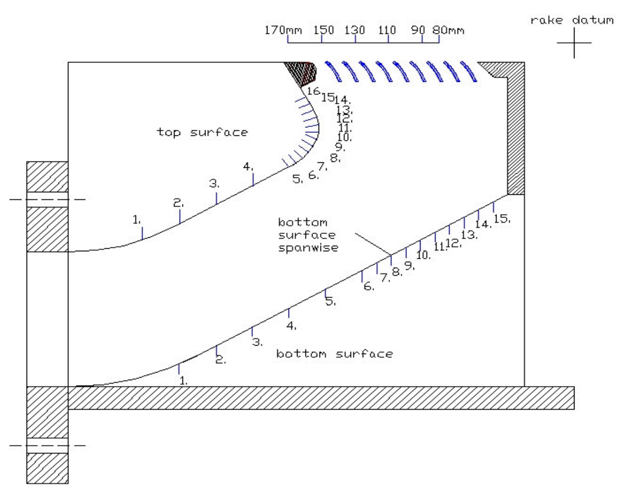

Figure 3. Positions of Static Ports and the Traverse of the External Pressure Rake.

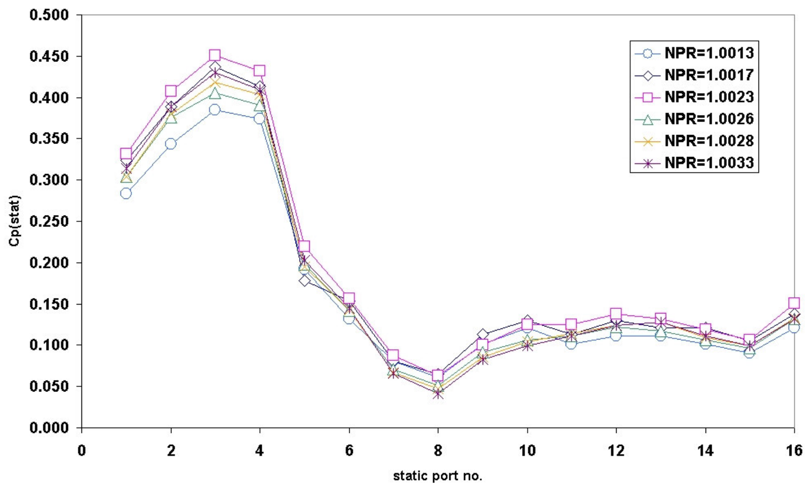

Figure 4. Top Wall Static Pressure Distribution.

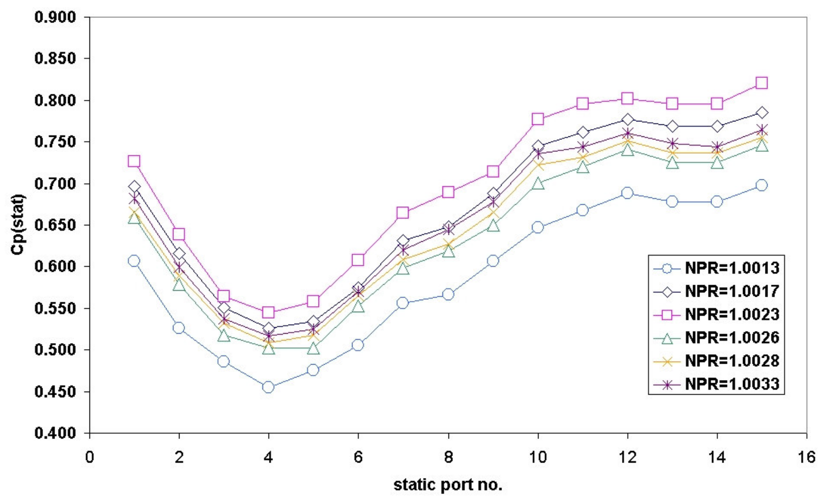

Figure 5. Bottom Wall Static Pressure Distribution.

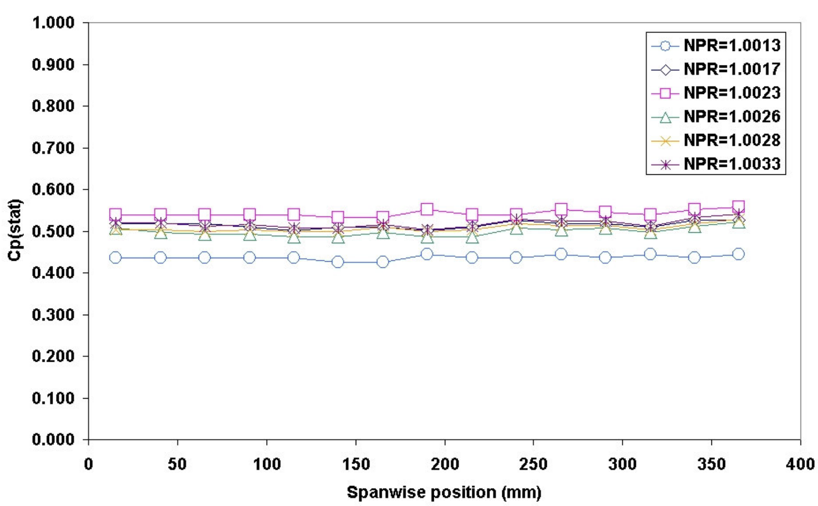

Figure 6. Bottom Wall Spanwise Static Pressure Distribution.

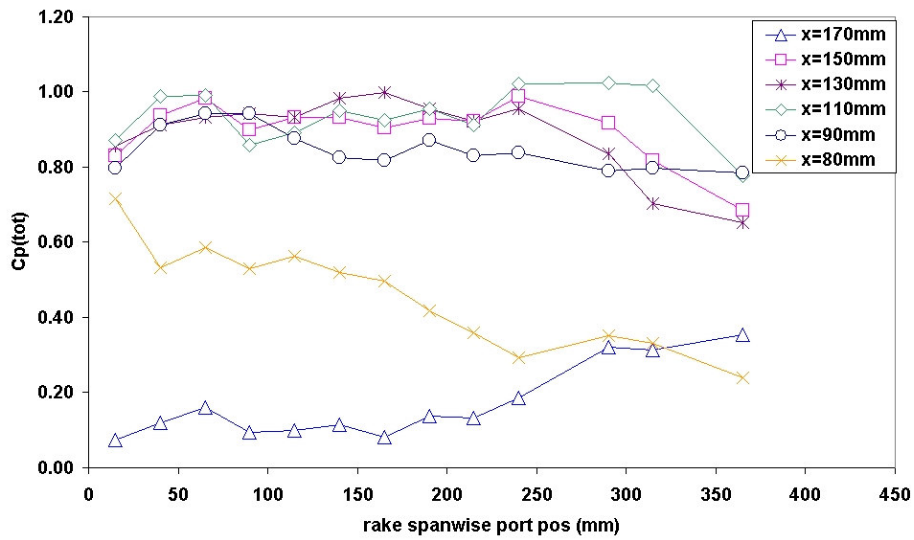

Figure 7. Post-Exit rake Total Spanwise Pressure Distribution.

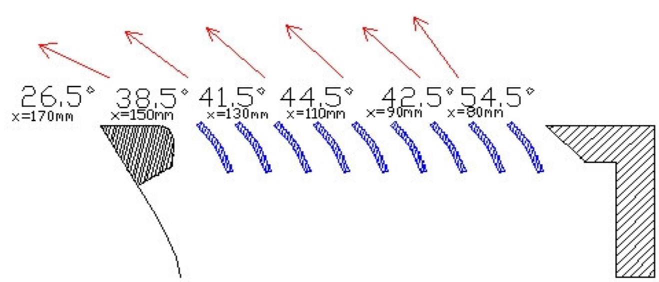

Figure 8. Post-Exit Rake Flow Direction at Centre-Span.

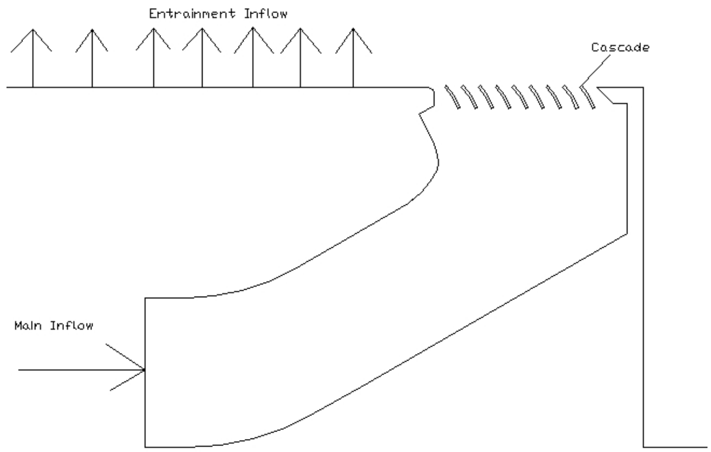

Figure 9. Detail of CFD Model Geometry

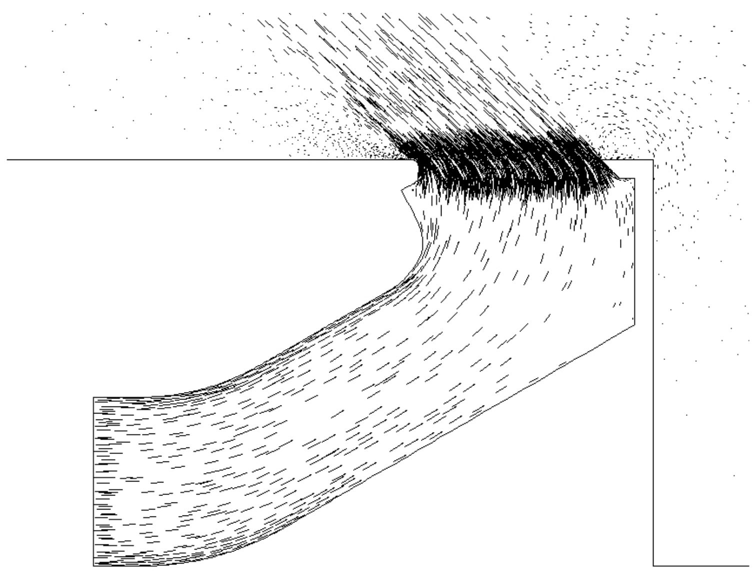

Figure 10. Velocity Vectors in the Thrust Reverser.

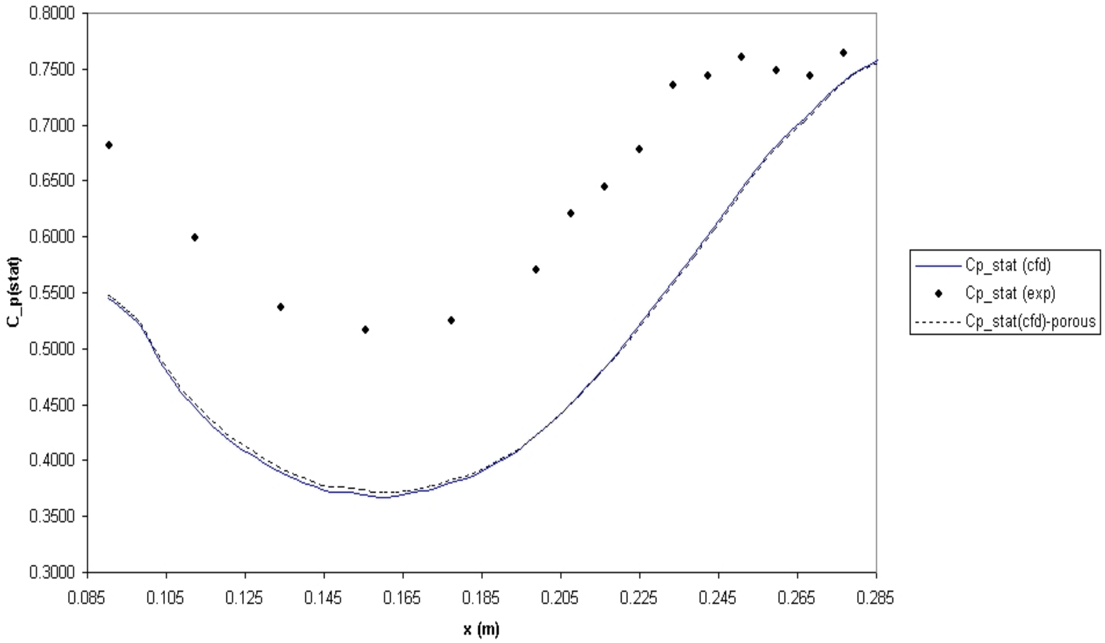

Figure 11. Comparison of Static Pressure Distribution on Bottom Wall.

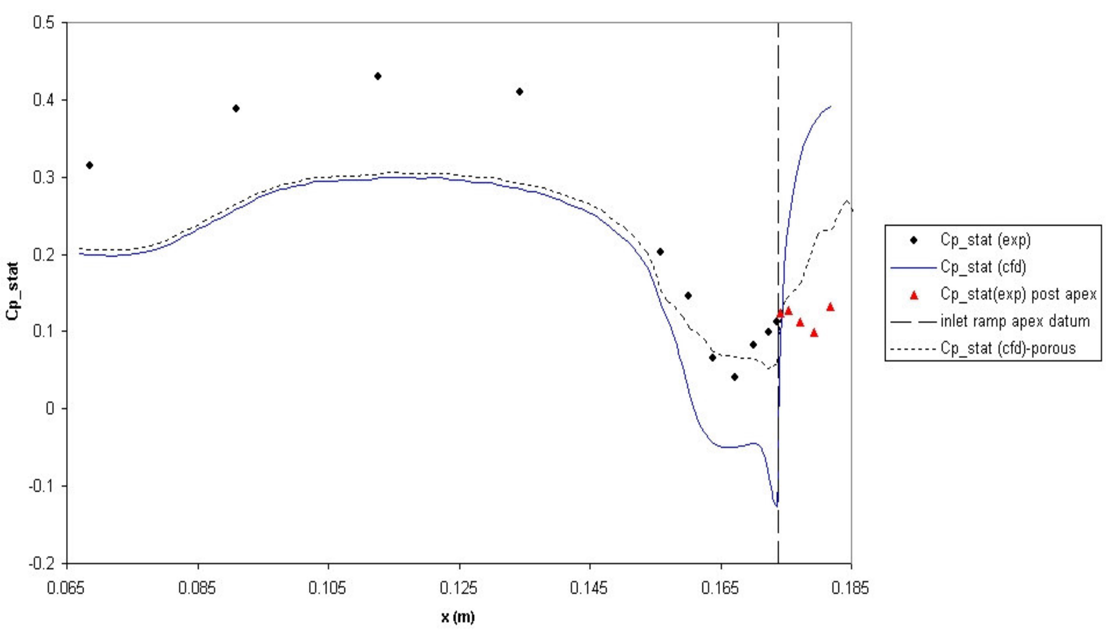

Figure 12. Comparison of Static Pressure Distribution on Top Wall.